Coseismic and post-seismic activity associated with the 2008 Mw 6.3 Damxung earthquake, Tibet, constrained by InSAR

Article *in* Geophysical Journal International · February 2014

DOI: 10.1093/gji/ggt444

CITATIONS
30

READS
281

4 authors, including:

Isabelle Ryder
University of Liverpool
46 PUBLICATIONS **1,183** CITATIONS

SEE PROFILE

Roland Burgmann
University of California, Berkeley
502 PUBLICATIONS **20,371** CITATIONS

SEE PROFILE

Geophysical Journal International

Geophys. J. Int. (2013) doi: 10.1093/gji/ggt444

Geophysical Journal International Advance Access published November 26, 2013

Coseismic and post-seismic activity associated with the 2008 M_w 6.3 Damxung earthquake, Tibet, constrained by InSAR

Lidong Bie,[1] Isabelle Ryder,[1] Stuart E.J. Nippress[2] and Roland Bürgmann[3]

[1] *School of Environmental Sciences, University of Liverpool, Liverpool, UK. E-mail: i.ryder@liv.ac.uk*
[2] *AWE Blacknest, Reading, UK*
[3] *Berkeley Seismological Laboratory, University of California, Berkeley, CA* 94720*, USA*

Accepted 2013 October 28. Received 2013 October 24; in original form 2013 May 30

SUMMARY

The 2008 M_w 6.3 Damxung earthquake on the Tibetan Plateau is investigated to (i) derive a coseismic slip model in a layered elastic Earth; (ii) reveal the relationship between coseismic slip, afterslip and aftershocks and (iii) place a lower bound on mid/lower crustal viscosity. The fault parameters and coseismic slip model were derived by inversion of Envisat InSAR data. We developed an improved non-linear inversion scheme to find an optimal rupture geometry and slip distribution on a fault in a layered elastic crust. Although the InSAR data for this event cannot distinguish between homogeneous and layered crustal models, the maximum slip of the latter model is smaller and deeper, while the moment release calculated from both models are similar. A ∼1.6 yr post-seismic deformation time-series starting 20 d after the main shock reveals localized deformation at the southern part of the fault. Inversions for afterslip indicate three localized slip patches, and the cumulative afterslip moment after 615 d is at least ∼11 per cent of the coseismic moment. The afterslip patches are distributed at different depths along the fault, showing no obvious systematic depth-dependence. The deeper of the three patches, however, shows a slight tendency to migrate to greater depth over time. No linear correlation is found for the temporal evolution of afterslip and aftershocks. Finally, modelling of viscoelastic relaxation in a Maxwell half-space yields a lower bound of 1×10^{18} Pa s on the viscosity of the mid/lower crust. This is consistent with viscosity estimates in other studies of post-seismic deformation across the Tibetan Plateau.

Key words: Time-series analysis; Seismic cycle; Radar interferometry; Earthquake source observations; Rheology: crust and lithosphere; Asia.

1 INTRODUCTION

On 2008 October 6, a M_w 6.3 earthquake occurred in the Damxung area of Tibet in western China. This event locates in the central part of the Yadong-Gulu rift system (Fig. 1), which extends about 500 km from Yadong in the Himalayan area up to the Gulu basin in central Tibet (Armijo *et al.* 1986). The NNE-trending, east-dipping boundary normal fault at the western side of the rift was suggested by Wu *et al.* (2011) as the source fault, according to analysis of isoseismal contours and aftershock distribution. However, detailed studies with various InSAR data (Elliott *et al.* 2010; Sun *et al*. 2011; Liu *et al.* 2012) lead to a different view that the fault causing the earthquake is a west-dipping secondary fault on the other side of the graben.

The Yadong-Gulu rift has long been characterized by moderate to large earthquakes. Last century, the 1952 M 7.5 earthquake struck the northern part of this rift at the Gulu Basin, and the 1992 M_w 6.2 earthquake hit Nyemu County immediately to the SW of the 2008 event. The 1411 AD M 8.0 earthquake is the largest one ever documented along this rift (Liu *et al.* 2012). Determination of accurate source parameters for the 2008 Damxung event is important for understanding local seismic risk and tectonic activity.

Detailed analysis and modelling of seismic data from project INDEPTH II (International Deep Profiling of Tibet and the Himalaya), which extends from the Tethyan Himalaya, across the Yarlu-Zangbo suture, to the centre of the Lhasa terrane, reveals that the upper crust in this region consists of layers with different velocities and that a low-velocity mid- to lower crust exists beneath ∼15 km (e.g. Nelson *et al*. 1996; Yuan *et al.* 1997; Kola-Ojo & Meissner 2001; Klemperer 2006). Klemperer (2006) also summarized the magnetotelluric (MT) studies across the plateau and interpreted the high electrical conductivity as induced by partial melt and/or saline aqueous fluids. Rippe & Unsworth (2010) related the high conductivity of mid- to lower crust to effective viscosities of 2.5×10^{18} to 3.0×10^{20} Pa s for the southern part of the Lhasa block. It would be of interest to obtain a constraint on the mid/lower crustal viscosity at this region from modelling of the InSAR observed post-seismic deformation.

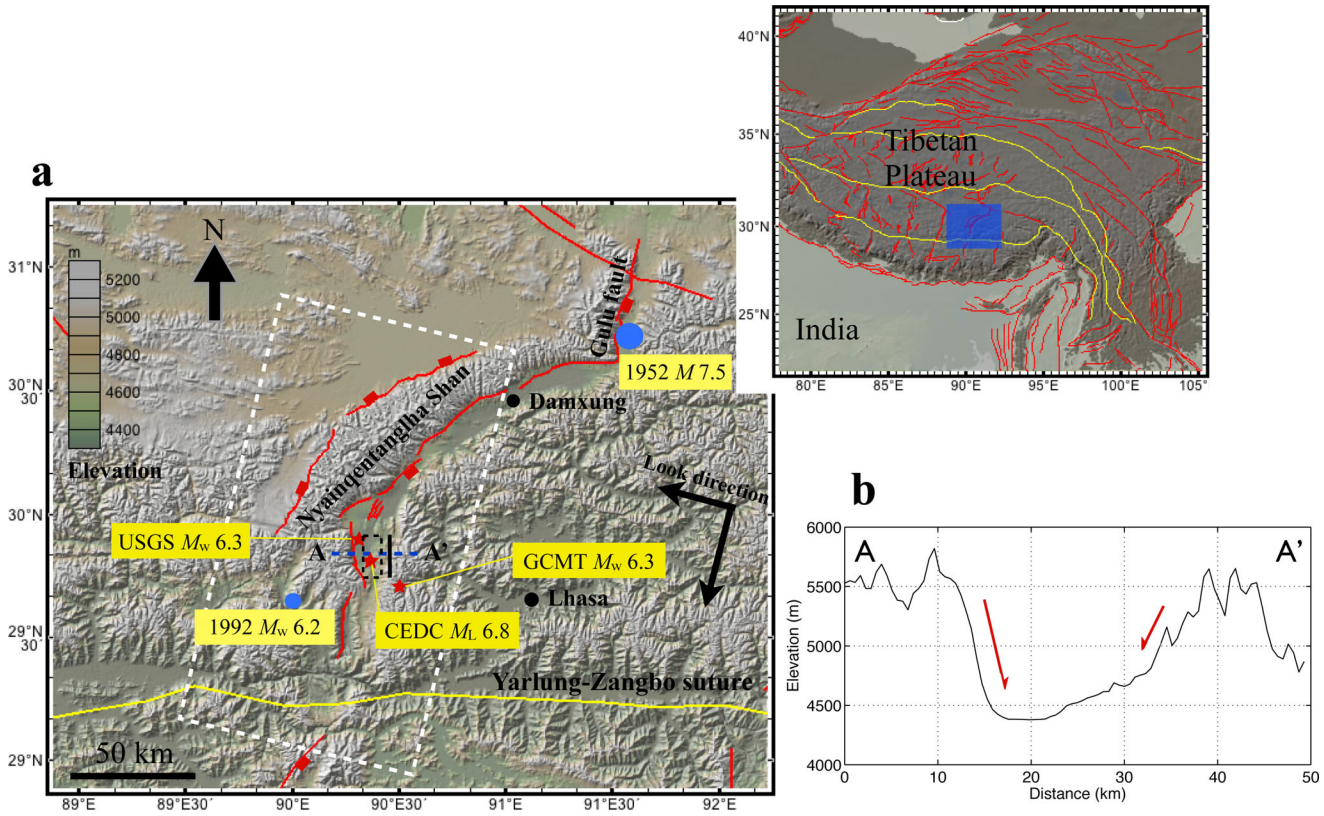

Figure 1. (a) Earthquake location (red stars, marked by catalogue name and magnitude) and shaded relief topography for the Damxung area. SRTM DEM (Farr *et al.* 2007) at 90 m resolution is shown. Red lines mark fault traces compiled by Styron *et al.* (2010). The Yarlung-Zangbo suture zone is delineated by thick yellow line. Black line marks the main shock fault surface trace and dashed black rectangle is surface-projected dislocation determined by InSAR in this study. Envisat track 176 is marked by white dashed box. Two blue circles show the locations of the 1952 *M* 7.5 and 1992 M_w 6.2 earthquakes, and magnitude is scaled to dot size. Inset shows the regional setting of the study area (blue box). (b) Topographic profile across the rift, along blue line A–A′ in (a).

A number of thrust and strike-slip events around the globe have been examined geodetically to investigate (i) the mechanism responsible for observed post-seismic deformation; (ii) the relationship between afterslip and aftershocks and (iii) the rheology of the crust and/or upper mantle (e.g. Peltzer *et al.* 1996; Deng *et al.* 1998; Bürgmann *et al*. 2002; Pollitz 2005; Hsu *et al.* 2006; Johanson *et al.* 2006; Ryder *et al.* 2007). However, only a small number of studies have focused on normal-faulting events (e.g. Nishimura & Thatcher 2003; Gourmelen & Amelung 2005; Riva *et al.* 2007; Ryder *et al.* 2010; Copley *et al.* 2012; D'Agostino *et al.* 2012). Previous published studies of the 2008 Damxung earthquake have examined the coseismic slip distribution (e.g. Elliott *et al.* 2010; Sun *et al.* 2011; Liu *et al.* 2012). The 2008 event also offers an opportunity to study the spatio-temporal evolution of afterslip, to test whether afterslip is temporally correlated with aftershocks, and to constrain the lower bound of mid/lower crustal viscosity for this part of the rift.

In this paper, we present a new inversion for coseismic slip distribution from three interferograms spanning the earthquake, exploring faults buried in both a homogeneous and a layered crust. A post-seismic deformation time-series (2008 October–2010 June) covering 12 SAR acquisitions is constructed using 17 interferograms (Table S1), and inverted for transient afterslip on the fault ruptured by the earthquake at each epoch. Then the temporal evolution of afterslip is compared with that of aftershocks. Finally, a lower bound on viscosity of the mid/lower crust of southern Tibet is estimated by comparing observed InSAR displacements with those computed assuming a model of viscoelastic relaxation of coseismic stress changes.

2 DATA

2.1 Interferograms

SAR images used in this study are from the ESA's Envisat satellite, which operates at C-band, with wavelength ∼5.6 cm. Scenes for both coseismic and post-seismic analysis are from descending track 176. The Shuttle Radar Topography Mission (SRTM; Farr *et al.* 2007) DEM with 90 m resolution is used to remove the phase component contributed by the topography.

All interferograms are produced from SAR scenes with perpendicular baseline smaller than 150 m, using the ROI_PAC software (Rosen *et al*. 2004). DORIS orbital information is used to remove orbital contributions to the mapped displacement. Interferograms are unwrapped using a branch-cut method (a ROI_PAC classic unwrapper) based on Goldstein *et al.* (1988). Out of a total of 56 interferograms, we choose three with good coherence to conduct a coseismic inversion for distributed slip, and 17 to build up a time-series of post-seismic deformation (Fig. 2).

2.1.1 Correction of tropostatic noise and orbital error

The main limitation of low-amplitude tectonic signal detection using InSAR is that orbital error and atmospheric delay projected into the line-of-sight direction can be at the same level as tectonic signals, or even larger, reaching tens of centimetres (Zebker *et al.* 1997). To minimize these effects, we apply a joint correction to each interferogram. Before correcting orbital error and tropostatic

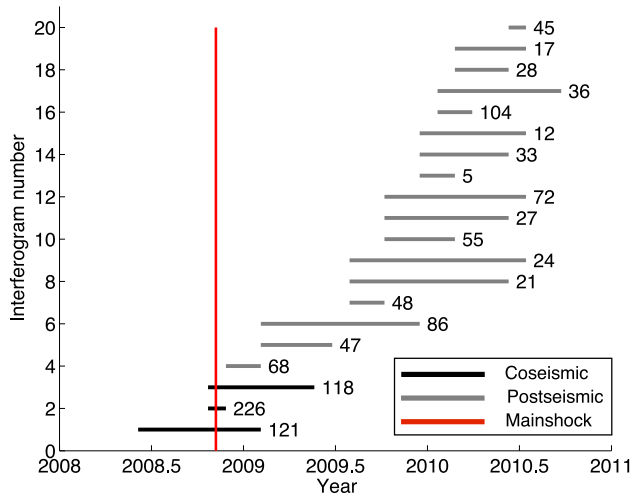

Figure 2. Time intervals covered by the co- and post-seismic interferograms, with perpendicular baseline in metres marked at the end of each line. The red bar denotes the time of the main shock.

delay, we first reference all post-seismic interferograms to the same point, and also manually fix small unwrapping errors as far as possible, in order to reduce the negative effect of unwrapping errors on estimating the correlation between phase change and topography. To minimize the effect of the residual orbital phase, we apply a first-order approximation of orbital error (Cavalié *et al.* 2007):

$$\varphi_{\text{orb}} = ax + by + cxy + d, \tag{1}$$

where x and y are range and azimuth coordinates, and a, b, c and d are constants for each interferogram that best fit the phase of the non-deformed area.

Atmospheric errors consist of propagation delay through tropospheric and ionospheric layers. Here we consider only tropospheric noise, because the ionospheric propagation delay is comparatively weak for the Envisat C-band data (Gray *et al.* 2000). Tropospheric delay is caused by temporal and spatial variations of the stratified troposphere and consists of two major components: a turbulent mixing effect due to laterally variable tropospheric properties, and a tropostatic effect due to temporal variation of stratified water vapour and the changing ratio of temperature to pressure in the troposphere (Hanssen 2001). To correct the tropostatic effect, a simple linear relationship between topography and phase change was proposed by Cavalié *et al.* (2007, 2008).

Jointly, we can write the interferometric phase (with deformed area masked out) due to residual orbital noise and tropospheric noise as a combination of both (Doin *et al.* 2009):

$$\varphi_{\text{orb+tropo}} = ax + by + cxy + d + kz, \tag{2}$$

where a, b, c, d and k are obtained by least squares inversion, x and y are range and azimuth coordinates, and z is elevation. Although the assumption of a linear relationship between elevation and atmospheric delay does not account for the non-stationary characteristic of atmospheric noise, applying this technique reduces the apparent noise.

We iteratively run the inversion for all interferograms. Then, according to eq. (2), we calculate the predicted noise, and finally subtract it from the interferogram. Corrected coseismic interferograms are then inverted for fault geometry and slip distribution, while corrected post-seismic interferograms are used to construct deformation time-series prior to inversion for afterslip.

As suggested by previous studies (e.g. Fialko *et al.* 2001; Sandwell *et al.* 2002; Simons *et al.* 2002), inversions incorporating interferograms with different look directions provide more reliable estimates of slip on the fault plane than those derived from only one look direction. However, in this study, the ascending data (Fig. S1) we obtained from ESA cover only part of the deformed area, and have relatively large noise (see also figs 5a and c in Sun *et al.* 2011). We therefore focus on data from descending track 176. We note that the coseismic interferograms in Figs 3(a)–(c) cover post-seismic periods (20, 90 and 215 d, respectively) as well as the earthquake itself, so there may be some post-seismic deformation included. In addition, a small component of the observed phase is related to non-tectonic noise, such as uncorrected atmospheric effects, orbital error, and DEM error. Fig. 3(d) shows displacement profiles crossing the fault trace. The maximum line-of-sight displacement in the hanging wall reaches 28 cm, while in the footwall, the negative line-of-sight displacement is only ∼5 cm. The asymmetry of the displacement profile is expected of dip-slip earthquakes.

2.2 Aftershocks

The aftershock dataset we use for temporal analysis is from the China Earthquake Data Centre (hereafter referred to as CEDC). It provides earthquake location, local magnitude and phase information free online (http://data.earthquake.cn/data/). Among the recorded aftershocks, most occurred within 100 d following the main shock (Fig. 4). We compare the temporal evolution of post-seismic slip and aftershocks, considering events until 2010 August 31.

Fig. 4 shows the number of CEDC-recorded aftershocks, $n(t)$, as a function of time t for the first year following the main shock. The curve fit to aftershocks (between the third day to the end of the first year since the main shock) using the a power-law equation:

$$n(t) = k(c + t)^{-p}, \tag{3}$$

where k, c, p are constants, gives a p value of 1.24. The p value falls near the higher end of the typical range of other aftershock sequences (Dieterich 2007), but we note that it is lower than for the L'Aquila event (D'Agostino *et al.* 2012), another moderate-size normal faulting earthquake. The two largest aftershocks occurred on 2008 October 6 and 2008 October 8, with local magnitude 5.5 and 5.7, respectively. The cumulative moment released by the first year of aftershocks is 4.68×10^{17} N m, which represents 13 per cent of the energy released by the main shock. The cumulative aftershock moment during the period spanned by the post-seismic data is only 5 per cent.

3 COSEISMIC SLIP INVERSION METHOD

From the noise-corrected co-seismic interferograms, we aim to estimate the following source parameters for the Damxung earthquake: location (centre of fault trace), strike, dip, rake, upper and lower depth of the fault, fault length and slip. Both a homogeneous elastic half-space (Okada 1985) and a layered elastic half-space (Wang *et al.* 2003) are considered. For both earth models, we first carried out a non-linear inversion to estimate all of the fault parameters listed above, with uniform slip across the fault plane. We then carried out a linear inversion for distributed slip, holding other parameters fixed.

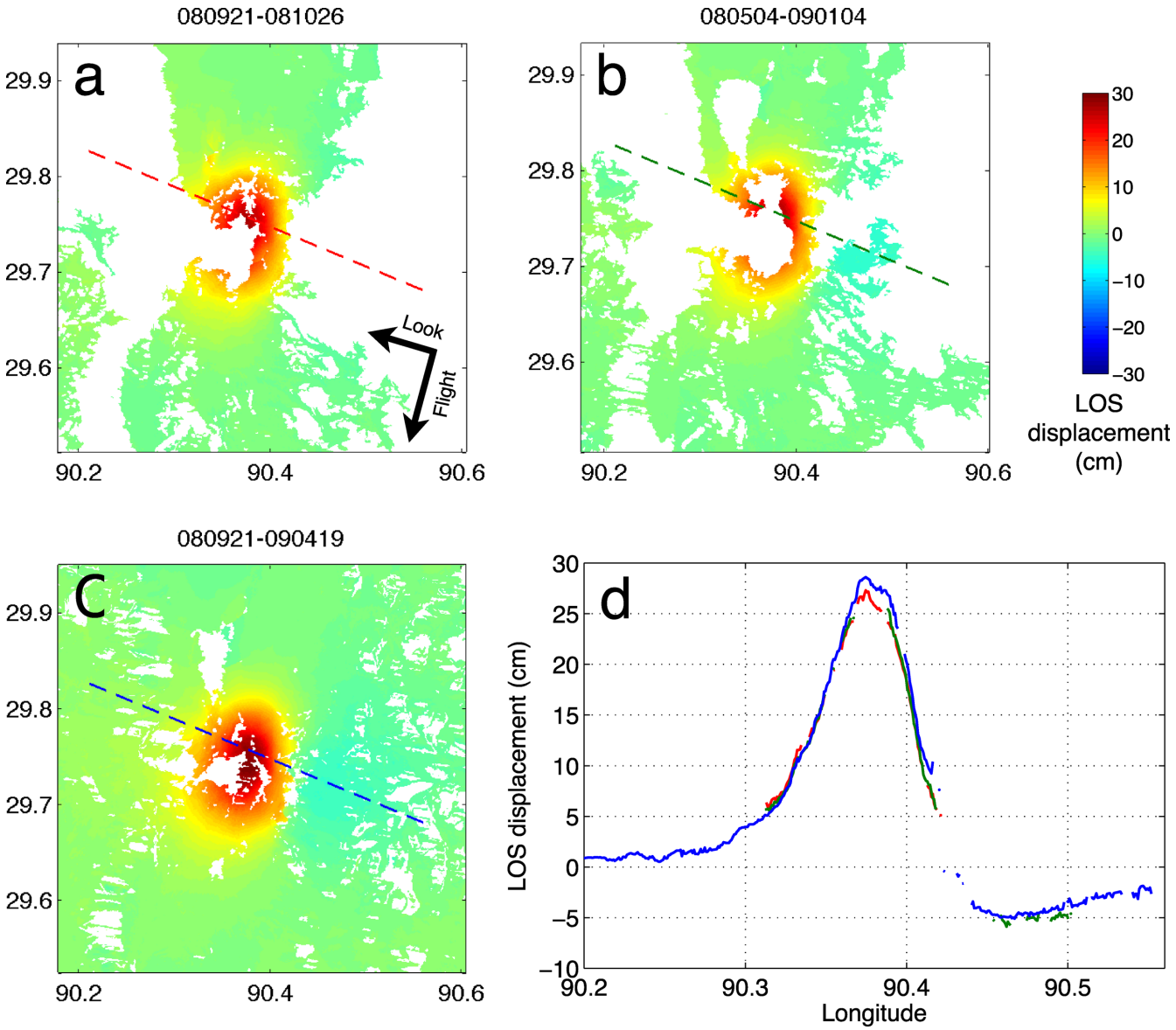

Figure 3. (a)–(c) Coseismic interferograms inverted for coseismic slip. Long and short arrows in (a) show descending satellite flight direction and look direction, respectively. SAR acquisition dates are shown above each interferogram in yymmdd format. Positive range change represents motion away from the satellite, while negative range change indicates motion towards the satellite. (d) Profiles showing coseismic line-of-sight displacement through the centre of the deformed area. Red, green and blue displacement profiles include 20, 90 and 215 d of post-seismic deformation, respectively (Fig. 2).

3.1 Homogeneous crust

3.1.1 Uniform slip model

We first assume uniform coseismic slip on a rectangular plane in an elastic half-space. The three unwrapped coseismic interferograms are down-sampled using a quadtree algorithm (Jónsson *et al.* 2002) to give 4793 pixels in total, greatly reducing the computational effort in the inversion. The influence of residual spatially correlated atmospheric noise is accounted for by the weighting matrix derived from Cholesky factorization (Harris & Segall 1987) of the inverse of the data covariance matrix. The covariance matrix is calculated from the 1-D covariance equation that best describes the autocorrelation between every pair of pixels at a given distance in the non-deforming area (Lohman & Simons 2005). A simulated annealing algorithm (Jónsson *et al.* 2002) is employed to find the global optimal model that minimizes the objective function, which is the sum of squares of weighted residuals (observed minus predicted displacements). The downhill simplex method (Nelder & Mead 1965) is used to test models returned by the simulated annealing method to avoid local minima (Wright *et al.* 1999). The optimal model is listed in Table 1. To determine parameter errors (e.g. Funning *et al.* 2005; Devlin *et al.* 2012), 100 simulated sets of spatially-correlated noise (Wright *et al.* 2003) are added to the displacement data, and then the optimal model is derived for each of the perturbed data sets using the hybrid simulated annealing and downhill simplex algorithm. Parameter errors are estimated from the obtained distributions by taking the standard deviations (Fig. S2).

3.1.2 Distributed slip model

Although residuals for the uniform slip model are generally small, as discussed in Section 5.1, we see localized residuals near the fault,

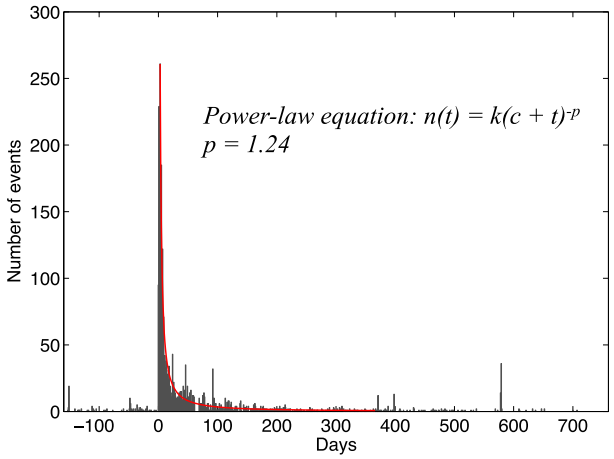

Figure 4. Number of seismic events in the range N29.25°–30.25°, E90.00°–90.70° that occurred between 2008 May 1 and 2010 August 31 as a function of time. Red line is a power-law fit to the first year of aftershocks, from the third day (with maximum number of aftershocks) after the main shock onwards. All events are taken from the China Earthquake Data Centre (http://data.earthquake.cn/data/).

especially around the southern end. To reduce residuals and obtain a more realistic slip model with distributed slip, we solved for slip on multiple fault patches using a linear inversion approach.

We initially fixed the rake at the value derived from the uniform slip model. Fault orientation parameters (location, strike and dip) were also fixed. We impose a non-negative slip constraint to obtain the slip distribution on the fault plane. The fault length and downdip width were extended, then the plane was discretized into 19 along-strike and 20 downdip patches, each with size 1 km × 1 km. Using the Okada elastic dislocation model (Okada 1985), a Green's function matrix was calculated, which contains the predicted line-of-sight changes at each location in the displacement data set produced by unit slip on each fault patch. The Laplacian operator was used to smooth the slip solution, and its effect was controlled by the smoothing factor, k, which also controls a constraint of zero slip on the side and lower edges of the fault plane (Jónsson *et al.* 2002). A resolution test (Fig. S3) indicates that slip at shallow downdip depth (0–5 km) can be well resolved in spatial pattern and amplitude, while slip at intermediate depth (5–11 km) is generally well recovered (small smearing with surrounding patches). Deeper slip patches (12–20 km) are smeared to a greater extent and may be mislocated.

We also solve for the slip vector by allowing variable rake. From the uniform slip modelling, we infer that the rake is between –45° and –135°. So, by calculating Green's functions for unit slip in these two end-member directions, the component of slip in each direction can be estimated (e.g. Ryder *et al.* 2010). Through vector calculation, we obtained both the direction and magnitude of slip on each fault patch.

3.2 Layered crust

The models described above consider the crust as a homogeneous elastic half-space, using the Okada model (Okada 1985). The effect of the layered elastic structure of the Earth on inversion of geodetic data has been widely discussed and tested (e.g. Savage 1987; Wald *et al*. 1996; Simons *et al.* 2002; Amoruso *et al*. 2004; Fialko 2004; Zhao *et al.* 2004; Hearn & Bürgmann 2005). It is generally found that incorporating depth dependence of elastic moduli can increase estimates of centroid depth and estimated moment compared to those obtained for an Okada half-space model. Thus, we consider local seismic velocity structures proposed by various studies outlined below, and implement an inversion for a layered crust.

Yuan *et al.* (1997) used recordings from INDEPTH II, GEDEPTH (German Depth Profiling of Tibet and the Himalayas) and the permanent broad-band Lhasa station to image the lithospheric structure of southern Tibet. The key feature of the velocity profile at station A36 (closest to the fault trace) is: a crustal low-velocity zone north of the Yarlu-Zangbo suture (at depths ∼13–30 km); a Moho depth of 70–80 km; and an *S*-wave velocity of ∼2.6 km s^{-1} down to a depth of ∼2.5 km, and ∼3.5 km s^{-1} at greater depths down to ∼13 km (refer to fig. 5 of Yuan *et al.* 1997). Kola-Ojo & Meissner (2001) compared a velocity profile derived from GEDEPTH data with that at A36 from Yuan *et al*. (1997), showing a much lower *S*-wave velocity in the upper ∼20 km of crust (refer to fig. 5 of Kola-Ojo & Meissner 2001). Using surface wave dispersion analysis, Rapine *et al.* (2003) found significant variation in the crustal velocity structure of southern and northern Tibet. The Lhasa terrane (where the 2008 Damxung earthquake occurred), with an S wave velocity of 2.75 km s^{-1} in the upper ∼5 km, has a low-velocity zone of 3.35 km s^{-1} in the middle crust between 20 and 30 km (refer to fig. 6 of Rapine *et al.* 2003).

Table 1. Source parameters derived from joint inversion of three Envisat interferograms, assuming uniform slip on rectangle buried in homogeneous and layered crust. InSAR results (Elliott *et al.* 2010; Liu *et al.* 2012) and seismic source parameters are also listed for comparison.

Parameters	Homogeneous crust (this study)	Layered crust (this study)	Homogeneous crust (Liu *et al*. 2012)	Homogeneous crust (Elliott *et al*. 2010)	USGS	GCMT
X (km)[a]	0.45 ± 0.05	0.76 ± 0.30	0.26 ± 0.02	0.58 ± 0.1	–18.73	7.36
Y (km)[a]	2.87 ± 0.11	2.55 ± 0.71	2.42 ± 0.05	3.55 ± 0.1	24.62	–7.54
Strike (°)	179.4 ± 0.5	180.0 ± 2.3	182.2 ± 0.2	181 ± 1	180	178
Dip (°)	54.8 ± 0.6	54.1 ± 2.9	54.4 ± 0.3	47 ± 1	48	53
Rake (°)	–114.6 ± 1.8	–108.4 ± 12.1	–111.7 ± 0.7	–115 ± 2	–119	–122
Top (km)[b]	5.18 ± 0.09	5.63 ± 0.46	4.54 ± 0.04	4.0 ± 0.1	–	–
Bottom (km)[b]	10.30 ± 0.21	10.47 ± 1.55	10.95 ± 0.05	10.7 ± 0.2	–	–
Length (km)	8.81 ± 0.14	8.99 ± 0.80	9.58 ± 0.07	10.4 ± 0.2	–	–
Slip (m)	1.76 ± 0.10	1.90 ± 0.55	1.33 ± 0.02	1.0	–	–
Moment (10^{18} N m)	3.13 ± 0.18	3.29 ± 0.95	3.23	3.1 ± 0.1	3.4	3.65

[a]X,Y are the central coordinates of the fault's upper edge projected to the surface. Reference point is at N29.728 E90.424.
[b]Top, bottom are the depth of the upper and lower edge of the fault plane, respectively.

Table 2. Seismic velocity and density structure for the simplified elastic crustal model, which consists of two layers, an upper layer with low velocity and a lower elastic half-space with higher velocity.

Layer no.	Thickness (km)	V_p (km s^{-1})	V_s (km s^{-1})	Density (g cm^{-3})	Rigidity (GPa)	Young's modulus (GPa)
1	4	4.75	2.74	2.29	17.19	43.00
2	Infinite	6.02	3.47	2.69	32.39	81.05

Taking the above studies into consideration, we construct a simplified model as follows: an upper layer, 4 km thick with low seismic velocities, overlying an elastic half-space with higher velocities. Table 2 summarizes the model parameters. The V_p/V_s ratios are consistent with a Poisson's ratio of 0.25 (Owens & Zandt 1997; Kind *et al*. 2002). Layer densities (ρ) are estimated from an empirical velocity–density relationship (Berteussen 1977):

$$\rho = 0.77 + 0.32 \times V_p, \quad (4)$$

To account for the layered nature of the crust, we utilize the software EDGRN/EDCMP (Wang *et al.* 2003), instead of the commonly used Okada model (Okada 1985), in the objective function to calculate line-of-sight displacements. It is demonstrated that the improved algorithm can retrieve synthetic source parameters well (see Table S2 and Fig. S4 for details of the test). The Fortran code EDGRN/EDCMP was developed by Wang *et al.* (2003) to compute displacements due to slip on a rectangular dislocation in a layered elastic medium. It comprises two modules: EDGRN calculates Green's functions at different depths for specified observation locations, by superposing the effect of each point source. The required input includes *P*-wave velocities, *S*-wave velocities and densities for each layer. The thickness of each layer should also be specified. EDCMP reads Green's functions passed from EDGRN, and calculates static deformation at given positions according to the input fault parameters.

The modelling approach used for the layered case to derive distributed slip was otherwise the same as that used for the homogeneous case. Fault parameters (location, strike and dip) derived from the uniform-slip model (Fig. S5) assuming a layered crust were passed to the EDCMP module to build Green's functions. Here, the fault plane was also discretized into 1 km^2 squares. Following the computation of the Green's functions, the inversion procedure is the same as that described in Section 3.1.2 to derive a slip distribution for the homogeneous crust case.

4 POST-SEISMIC DEFORMATION TIME-SERIES AND AFTERSLIP INVERSION

We selected 17 differential interferograms (Table S1) with good coherence to construct post-seismic deformation time-series spanning 2008 October 26 to 2010 August 22, and consisting of 11 time intervals. Each unwrapped interferogram was down-sampled by a factor of 10. Next, a least squares inversion for line-of-sight distance change at every pixel during each time interval was performed using the following equation:

$$\begin{pmatrix} G \\ kT \end{pmatrix} m = \begin{pmatrix} d \\ 0 \end{pmatrix}, \quad (5)$$

where G is a matrix of ones and zeros referencing the interferogram time intervals, m is a vector of the displacement at each time that we need to derive, k is a temporal smoothing factor that controls the effect of the smoothing operator T and d is a vector of line-of-sight displacement (Berardino *et al.* 2002; Schmidt & Bürgmann 2003; Philibosian & Simons 2011; Barnhart & Lohman 2012). The smoothing operator T is a matrix constructed assuming a first-order linear increment of displacement in the time domain. By plotting residual sum of squares (RSS) misfit versus model time-series roughness for different smoothing factors, we chose the value that allows both parameters to be low. Pixels that cannot be solved by the system because of rank deficiency or insufficient finite values were assigned no value. The gap in SAR coverage between the event and first acquisition date was filled by extending the displacement backwards, assuming a linear displacement gradient for the first 21 d (Ryder *et al.* 2007). We note that the linear approximation likely underestimates the real displacement values by a small amount. Finally, line-of-sight displacement maps at successive dates with reference to the common scene were produced by summing displacements in appropriate time intervals.

Post-seismic deformation time-series reveal localized deformation on the southern part of the fault (Fig. 5). The maximum line-of-sight displacement reaches ~3 cm adjacent to the inferred coseismic fault trace in the hanging wall side one year after the earthquake. Together with the change in sign of line-of-sight displacements across the fault trace (Fig. 5), this information implies that afterslip on the fault plane that ruptured coseismically is the most likely mechanism responsible for the near field post-seismic deformation, rather than viscoelastic relaxation, which would produce a circular uplift across the fault as described in Section 6. The displacement in the footwall is not obvious, because its magnitude is much smaller than that in the hanging wall. An exponential fit of the form $A(1 - e^{-t/\tau})$ to the cumulative average displacement of the hanging wall pixels (boxed in Fig. 5) gives a decay time τ of ~227 d (Fig. 6).

We invert the time-series for cumulative time-dependent afterslip. We do not include the last epoch, which has relatively large noise on the hanging wall side of the fault. A model considering crustal layering is adopted, with the same velocity structure as that used in the inversion for the coseismic slip distribution (Table 2). Source parameters are inherited as the coseismic rupture from Section 3.2.

5 INVERSION RESULTS

5.1 Coseismic inversion

The model of uniform slip on a rectangular fault plane buried in a homogeneous crust reproduces the line-of-sight surface displacements well, with rms misfits of 1.43, 1.10 and 1.62 cm, respectively, for the three interferograms. Errors in inferred fault parameters are generally small (Table 1). The estimated fault plane strikes nearly north–south, dips to the west at 54.8°, and is buried with its top edge at a downdip depth of ~5 km. This result is consistent with other InSAR studies of the earthquake source parameters (Elliott *et al*. 2010; Sun *et al.* 2011; Liu *et al.* 2012), but differs from that deduced by Wu *et al.* (2011), who suggests that the east-dipping boundary fault ruptured based on seismicity and ground motion data. Uniform slip including crustal layering gives parameters of

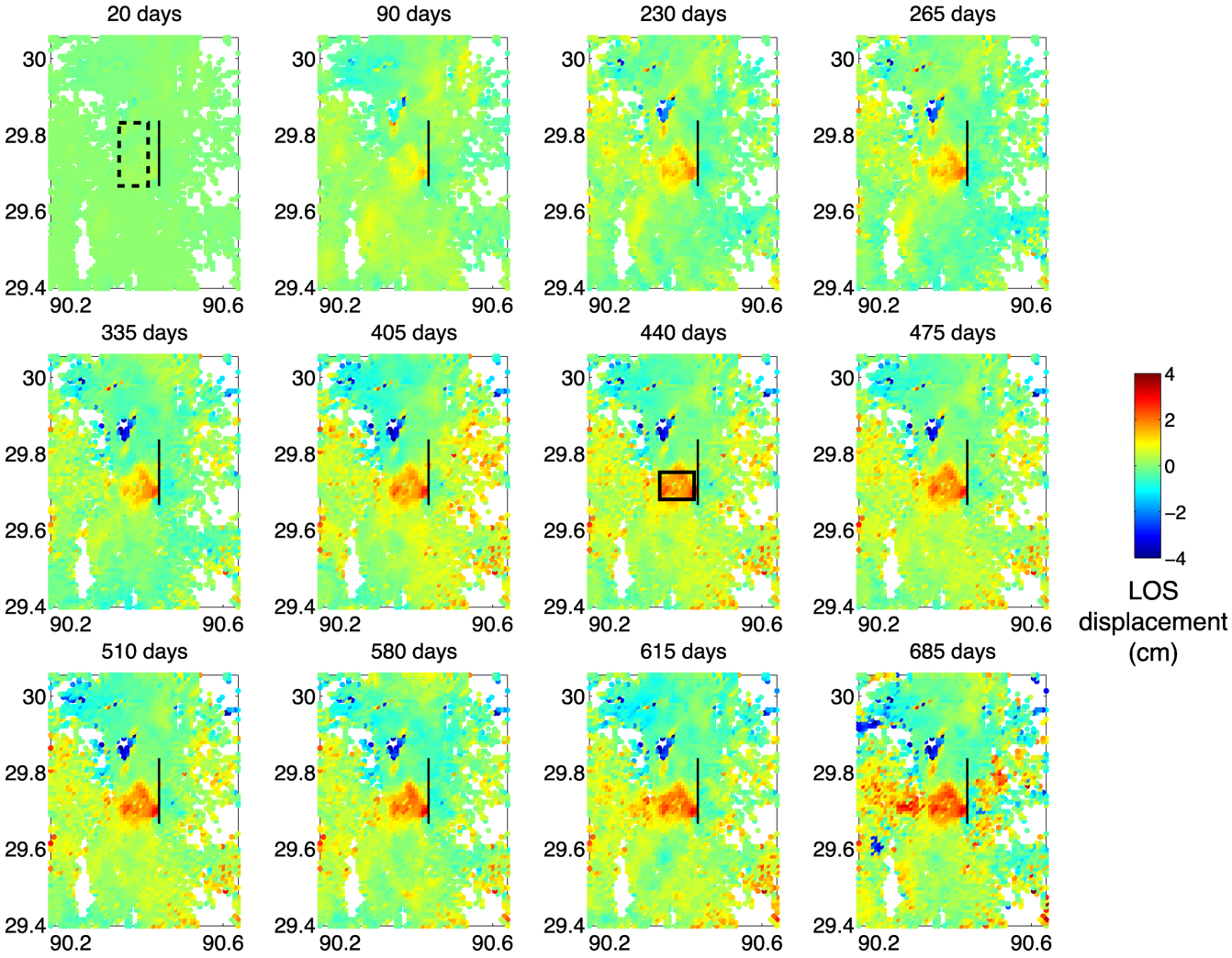

Figure 5. Post-seismic deformation time-series. The first panel is the linearly back-projected LOS displacement between the earthquake and the first SAR acquisition after the earthquake, with dashed box as the surface projection of the fault plane. Positive range change represents motion away from the satellite, while negative range change indicates motion towards the satellite. Black line represents the fault trace inferred in this study. Pixels in the black box on the hanging-wall (440 d deformation map) are averaged for cumulative line-of-sight displacement calculation in Fig. 6. Days refer to number of days after earthquake on 2008 October 6.

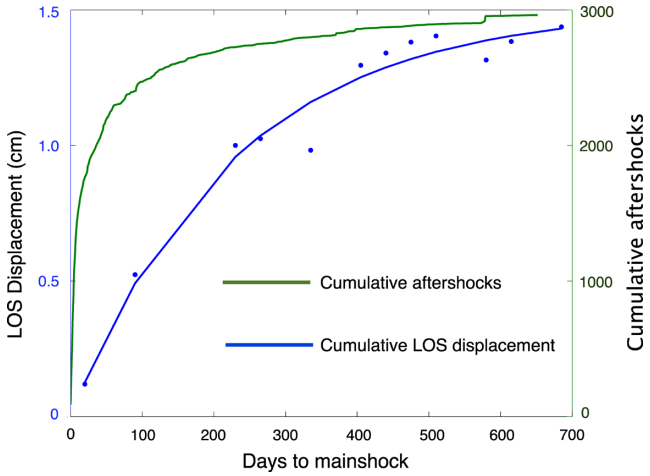

Figure 6. Cumulative number of aftershocks and cumulative line-of-sight post-seismic displacement as a function of time. Cumulative post-seismic displacement is the average value of pixels in the black box in Fig. 5.

fault location, strike and dip comparable to those derived from homogeneous crustal model. The rms misfits between predicted and observed displacement are 2.02, 1.46 and 1.43 cm for the three interferograms.

The distributed slip model with fixed rake positivity constraint generally shows the same slip pattern for both crustal models (Figs 7a and b). Slip greater than 1.0 m occurs mainly between 6 and 12 km downdip distance, but the peak slip from the homogeneous crust model is ∼30 cm larger than that from the layered crust model. Several patches on the shallow southern part of the fault show a maximum of 0.5 m slip. The rms misfits between predicted and observed displacement for the homogeneous crust model are 1.23, 1.07 and 1.44 cm, and 1.23, 1.06 and 1.45 cm for layered crust model.

The slip vector is solved for both crustal models (Figs 7d and e). Again, as for the model with fixed rake, the general slip patterns are similar: the primary slip patch tapers to the upper northern part of the fault. The maximum slip for the layered model is 2.22 m at a downdip depth of 9.5 km, and for the homogeneous model the maximum is 2.38 m at 8.5 km depth. The oblique slip on the

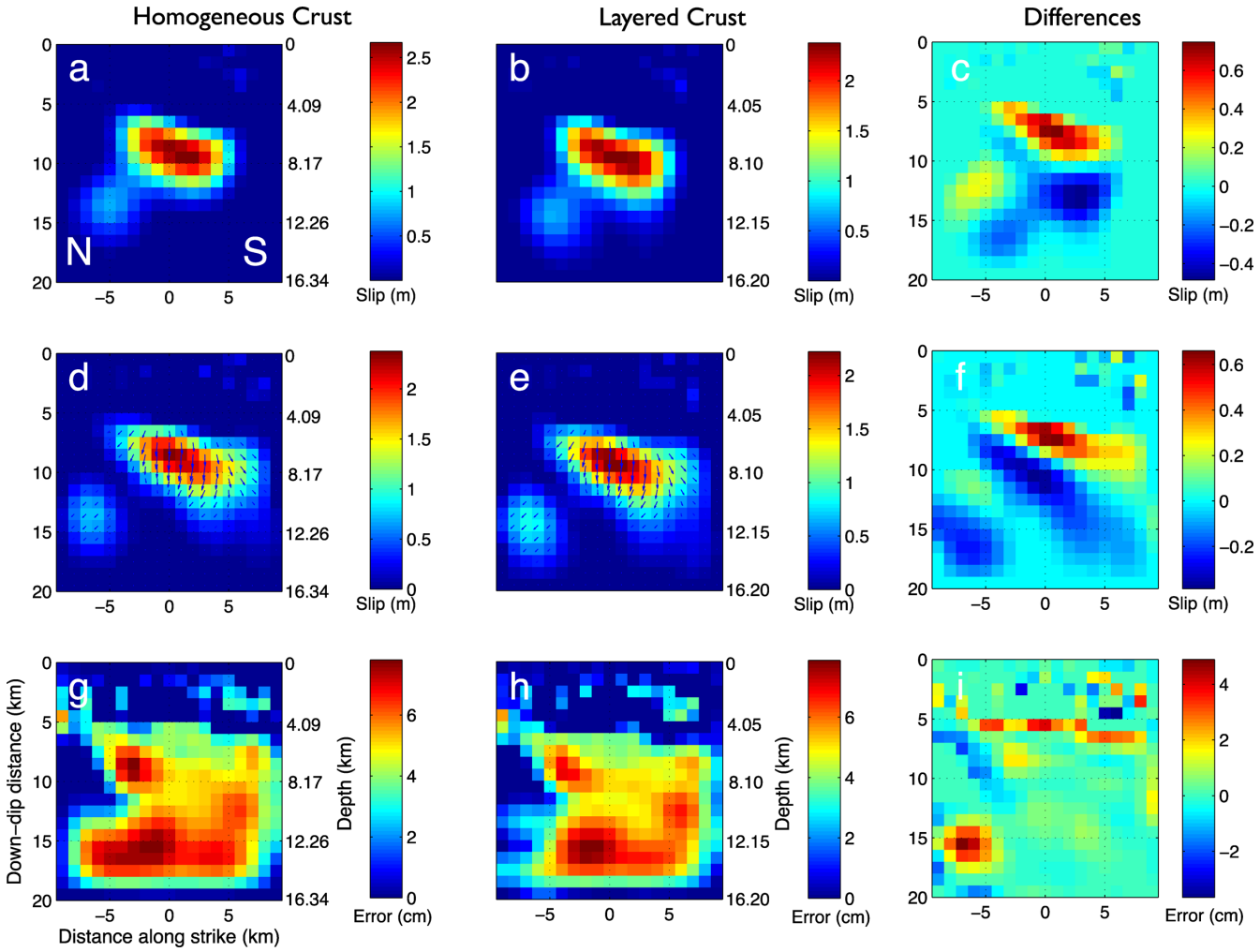

Figure 7. Modelled slip distribution on the fault plane. Panels (a) and (b) assume fixed rake and (c) is the difference between (a) and (b), while (d) and (e) assume variable rake with arrows marking the slip direction and (f) is the difference between (d) and (e). Panels (g) and (h) are estimated errors of distributed slip models with variable rake and (i) is the difference between (g) and (h). Panels on left are derived from homogeneous crust model and panels in the middle from layered crust model.

deep northern part of the fault plane may be an artefact caused by residual noise localized in the northern part of the hanging wall. We run the inversion 100 times to invert the 100 sets of realistic noise-perturbed data for slip distribution on each patch (Wright *et al.* 2003; Barnhart & Lohman 2013). The estimated error on each patch is one standard deviation of the derived 100 slip values. All errors are less than 8 cm (Figs 7g and h). The overall area of slip in the layered model is slightly larger and deeper than that for homogeneous one. The moment release of the layered crust slip model is 3.67×10^{18} N m, and 3.60×10^{18} N m for the homogeneous crust model, both equivalent to a M_w 6.3 earthquake. The rms misfits are slightly reduced relative to the fixed rake case: 1.20, 1.04 and 1.41 cm for the homogeneous crustal model, and 1.21, 1.03 and 1.42 for the layered model.

The above analysis demonstrates that the InSAR data for this event are not able to distinguish between homogeneous and layered crustal models, in terms of goodness of fit. This is possibly due to the fact that the coseismic slip is mainly buried beneath the upper low-rigidity layer. However, when the previously mentioned independent geophysical evidence for layering is taken into account, estimated slip is deeper and has smaller magnitude than for a homogeneous model.

Fig. 8 shows the observed and modelled coseismic line-of-sight displacements, as well as the residuals for the distributed slip model with variable rake in a layered crust. The hanging wall residuals for the three coseismic interferograms show a consistent trend, from negative in the date pair 2008 September 21–2008 October 26, nearly zero in 2008 May 04–2009 January 04, to positive in 2008 September 21–2009 April 19. This indicates that the slip model reproduces the second interferogram (2008 May 04–2009 January 04) best, and moderately overestimates the 'real' coseismic slip. The residuals for the coseismic interferogram spanning 215 d after the earthquake (2008 September 21–2009 April 19) show a positive line-of-sight displacement (consistent with additional subsidence) in the hanging wall of the rupture, which may suggest a contribution of afterslip that we explore in detail below. The negative residuals in the near field at the southern end of the fault may be a result of a simplified fault geometry.

5.2 Afterslip inversion

The afterslip inversion results show some stable spatial features (Fig. 9). Three patches A, B and C appear in all time-series epochs.

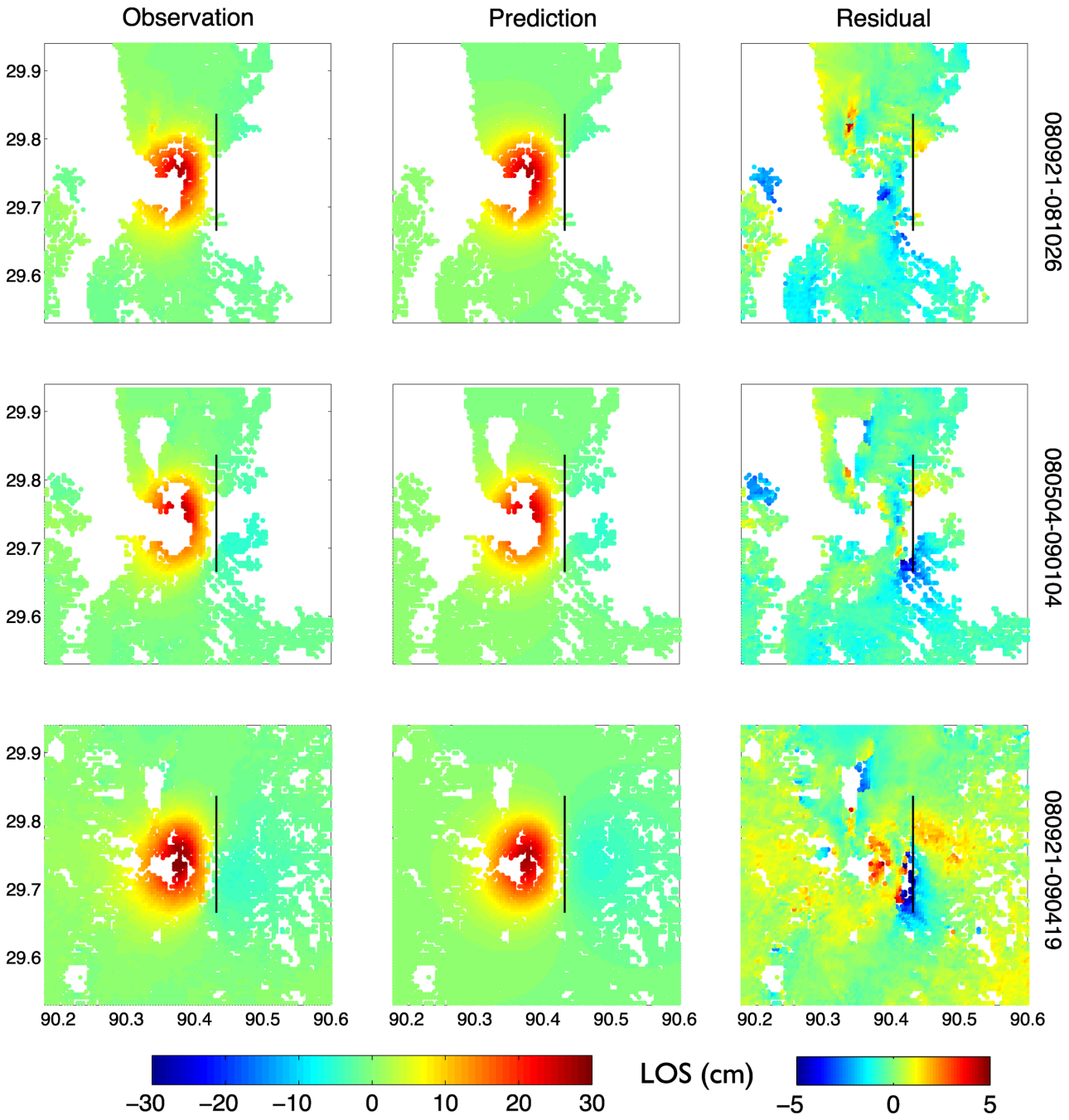

Figure 8. InSAR observations and model prediction from slip distribution model with variable rake in a layered crust. Residuals are shown in the third column. Black lines mark fault trace. SAR acquisition dates are in yymmdd format on the right side of each residual map. Positive range change represents motion away from the satellite, while negative range change indicates motion towards the satellite.

The shallowest patch A sits at the southern part of the fault, at a downdip distance of 3–5 km. This patch smears with the other two patches in the second to fifth epochs. Patch B is located at a downdip depth of 6–8 km, overlapping with the upper edge of the coseismic slip model. The third and largest patch C lies roughly downdip and just south of the rupture at 10–15 km depth. The spatial pattern of this deep-seated patch is not stable, as the third to fifth epochs show variable depth range, likely due to the fact that it is harder to consistently resolve this deeper slip patch.

The rms misfits between modelled and observed post-seismic displacements for each epoch are smaller than 0.73 cm. The post-seismic deformation time-series is satisfactorily reproduced (Figs S6 and S7). Afterslip errors are estimated by re-running the inversion of noise-perturbed time-series 100 times to obtain a slip value distribution for each patch. The standard deviation of each patch is plotted as a separate time-series in Fig. S8, showing that the spatial distribution of error is similar to that of afterslip. For patch A, the error is <10 cm. For patch B, the error does not increase significantly with time, and for patch C, the error is obviously larger than that for patches A and B, and increasing with time. The largest error for each epoch appears at variable depth on the most northern part of the fault. This may result from the residual atmospheric noise in the northwest part of the hanging wall being mapped into the slip distribution. Error calculation and analysis indicate that

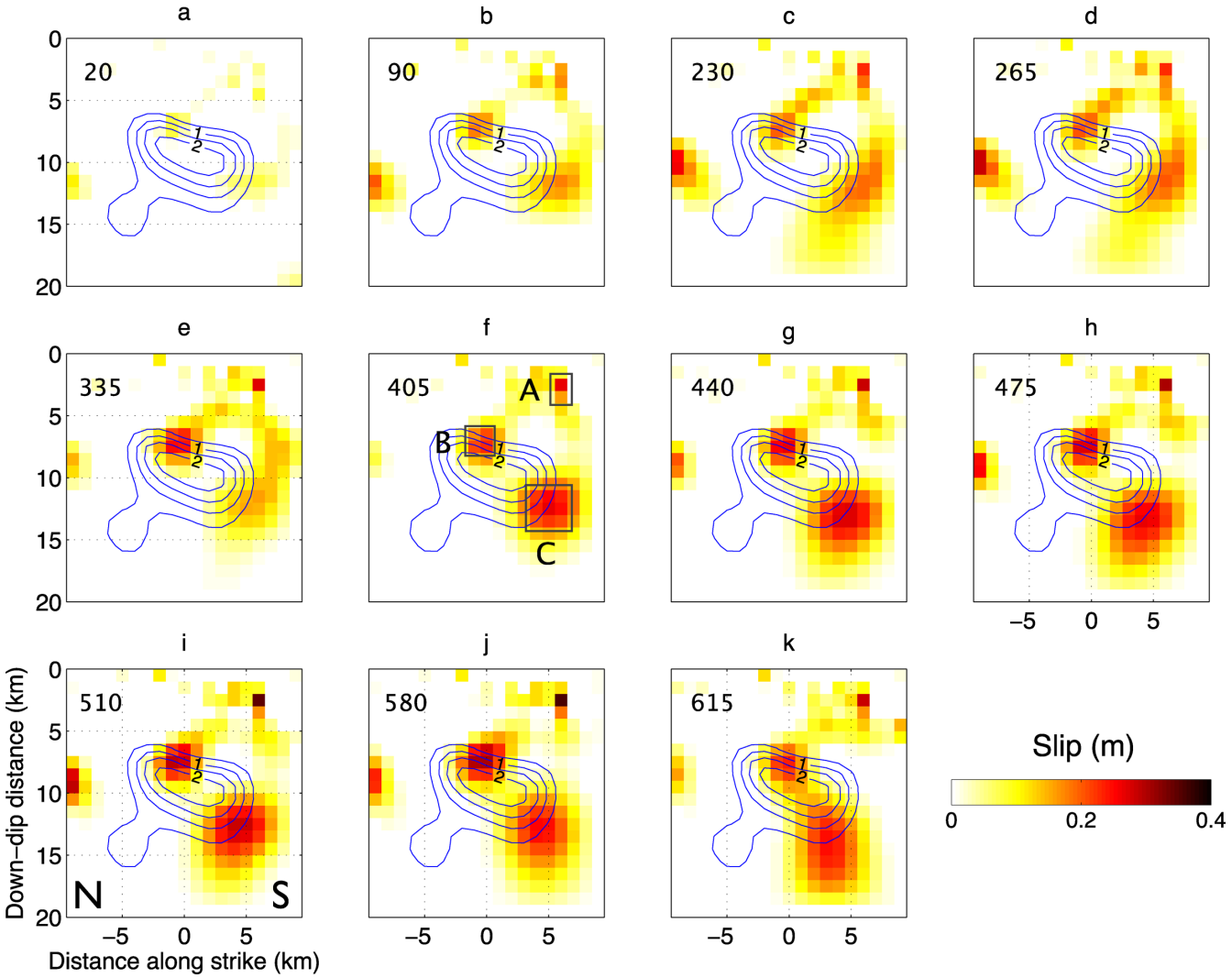

Figure 9. Cumulative transient afterslip estimated for the date of each post-seismic SAR acquisition using the layered model, compared with the coseismic slip distribution derived from the layered crust model with fixed rake (blue contours, labels in metres). A, B and C are three spatially stationary patches discussed in the text. Numbers at the upper left-hand corner indicate days since main shock.

afterslip patches A and B are well resolved, and when dealing with afterslip deeper than a downdip depth of 11 km, slip features should be treated with caution.

The upper two afterslip patches generally have not migrated much spatially over the timespan of observations. While there is an apparent tendency of patch C to migrate downwards along the fault plane with time (Fig. 9), as was inferred for the Izmit earthquake (Bürgmann *et al*. 2002), the fault slip is poorly resolved below the depth of 10–12 km (Fig. S3). Deeper afterslip (downdip depth >15 km) on the downdip extension of the coseismic rupture is not found.

The cumulative maximum slip averaged over the boxed elements shown in Fig. 9(f) after 615 d is ∼20 cm for all three patches (Fig. 10). The total afterslip moment is 3.76×10^{17} N m, which is ∼10 per cent of the moment inferred from coseismic interferograms. Exponential fits to the cumulative afterslip of the three patches give an increasing decay time with depth (Fig. 10). The overall moment release evolves with an exponential decay time of 154 d (Fig. 11). The obvious discontinuity of the moment release at 335 and 405 d after the main shock might be a result of overcorrection of atmospheric and orbital noise, which in turn may underestimate the afterslip. This underestimation can also be seen from the fits to averaged afterslip of each patch (Fig. 10). We should note that both afterslip and moment are expected to be larger than presented here, because the linear estimation of the first 20 d of deformation would likely have underestimated the initial post-seismic deformation.

6 VISCOELASTIC MODELLING

The mid/lower crustal and/or upper mantle viscosity of the Tibetan Plateau has been estimated from InSAR studies of several moderate to large earthquakes that occurred in recent years (e.g. Ryder *et al.* 2007, 2010, 2011; Wen *et al.* 2012; Yamasaki & Houseman 2012). However, the earthquakes studied are mainly strike-slip, and involve faults located generally in regions close to the margins of the Tibetan Plateau. Thus, the viscosity of the interior of Tibet is not well established. Here, we adopt the same method as used by Ryder *et al.* (2010) to constrain local strength beneath the elastic upper crust in southern Tibet.

We use the software PSGRN/PSCMP written by Wang *et al.* (2006) to simulate the post-seismic line-of-sight displacement due to viscoelastic stress relaxation. PSGRN/PSCMP shares the same

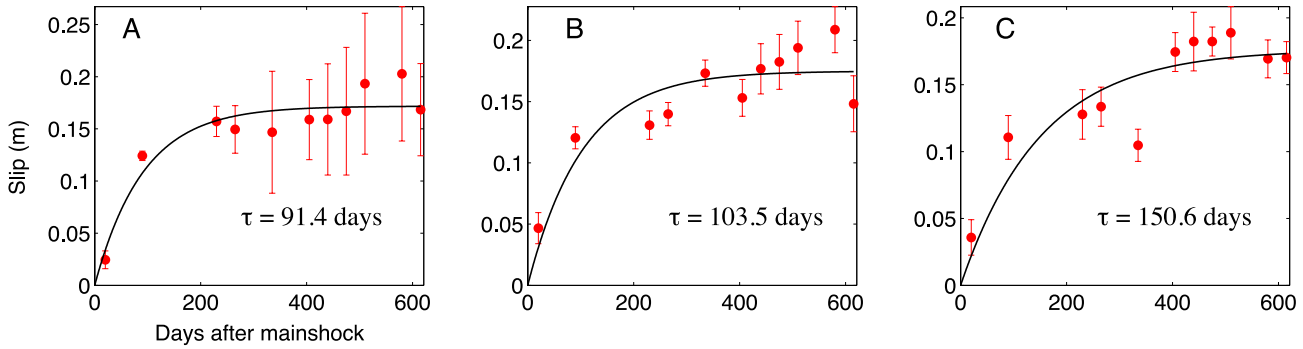

Figure 10. Afterslip evolution of patches A, B and C, with best-fitting exponential curve. The error at every epoch is the standard deviation of the slip magnitude for the patches boxed in Fig. 9(f).

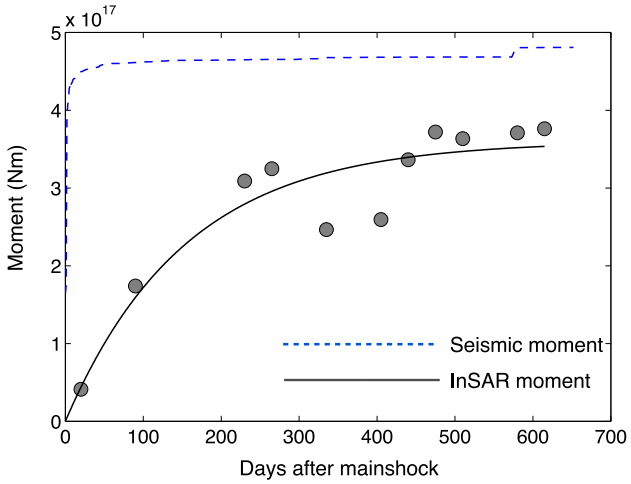

Figure 11. Time evolution of cumulative post-seismic moment released by afterslip (grey dots, with best-fitting exponential marked by black line) and aftershocks (blue dashed line).

workflow as the coseismic deformation modelling software EDGRN/EDCMP descried earlier. It includes two modules: PSGRN calculates Green's functions and PSCMP calculates post-seismic displacements at given time. In the PSGRN module, the user can input the seismic velocities and viscosities of different layers. The code is designed to implement a Burger's rheology, which is a Kelvin–Voigt body and a Maxwell body in series. To model Maxwell relaxation, the transient viscosity (dashpot of the Kelvin–Voigt body) is set as zero, while the steady state viscosity (dashpot of the Maxwell body) is non-zero (Wang *et al.* 2006). This software has been employed to study many earthquakes to infer lithospheric rheology from geodetic observations of post-seismic deformation (e.g. Barbot *et al.* 2008, 2010; Xiong *et al.* 2010; Hoechner *et al.* 2011; Wen *et al.* 2012).

In order to obtain a general idea of the post-seismic surface expression of viscoelastic relaxation below the seismogenic zone, we first run a forward model by inputting an arbitrary viscosity (1×10^{18} Pa s) of a Maxwell viscoelastic half-space under a 15-km-thick elastic upper crust. We use our coseismic slip model derived for a layered earth (Fig. 7e) and the rheology parameters shown in Table 3. We find that circular uplift is broadly distributed over the fault trace (Fig. 12c), while subsidence occurs in the far field, as is also evident for other normal-faulting earthquakes studied by

Table 3. Rheology structure used as input to PSGRN. A Maxwell half-space lies beneath a 15 km-thick upper crust that includes two layers with different velocities.

Layer no.	Thickness (km)	V_p (km s^{-1})	V_s (km s^{-1})	Density (g cm^{-3})	Viscosity (Pa s)
1	4	4.75	2.74	2.29	N/A
2	11	6.02	3.47	2.69	N/A
3	Infinite	5.85	3.38	2.75	1×10^{18}

Nishimura & Thatcher (2003), Gourmelen & Amelung (2005) and Ryder *et al.* (2010). The uplift is the surface response to material at depth flowing in towards the faulted area. In our post-seismic deformation time-series, we find no clear evidence of such uplift over the fault, so direct estimation of the optimal viscosity is not possible. However, we can still estimate a lower bound on the viscosity of the mid/lower crust, by running multiple viscoelastic models with different viscosities of the Maxwell half-space (Ryder *et al.* 2010).

The elastic layer thickness is set to 15 km (Ryder *et al.* 2007, 2010) and elastic parameters are the same as those used for the coseismic slip inversion in a layered earth. For a range of viscosities varying between 1×10^{16} and 2×10^{19} Pa s, we simulate the transient post-seismic displacements and calculate the rms misfit between the modelled viscoelastic displacements and the post-seismic deformation time-series. The modelled displacements for the 615 d epoch are shown in Figs 12(a)–(d), for viscosities of 10^{16}, 10^{17}, 10^{18} and 10^{19} Pa s, respectively. Figs 12 (e)–(h) show the residuals between cumulative line-of-sight displacement and modelled viscoelastic displacement for variable viscosities. When a larger viscosity is applied, the expected viscoelastic relaxation signal is smaller, leaving the residual as close as to the displacement caused by afterslip (e.g. Figs 12g and h) residual. The viscosity beneath which the rms misfit value begins to rise steeply is taken as the lower bound on the Maxwell viscosity (Ryder *et al.* 2010). Fig. 13 shows the rms misfit values as a function of viscosity. The rms misfit levels off at high viscosities, as the modelled displacements become insignificant with respect to the interferograms. The lower bound obtained is 1×10^{18} Pa s. Errors are the standard deviations of the rms misfit distributions derived by re-running the residual calculation 100 times for noise-perturbed deformation time-series. The errors in rms misfit values are generally smaller than ~0.023 cm.

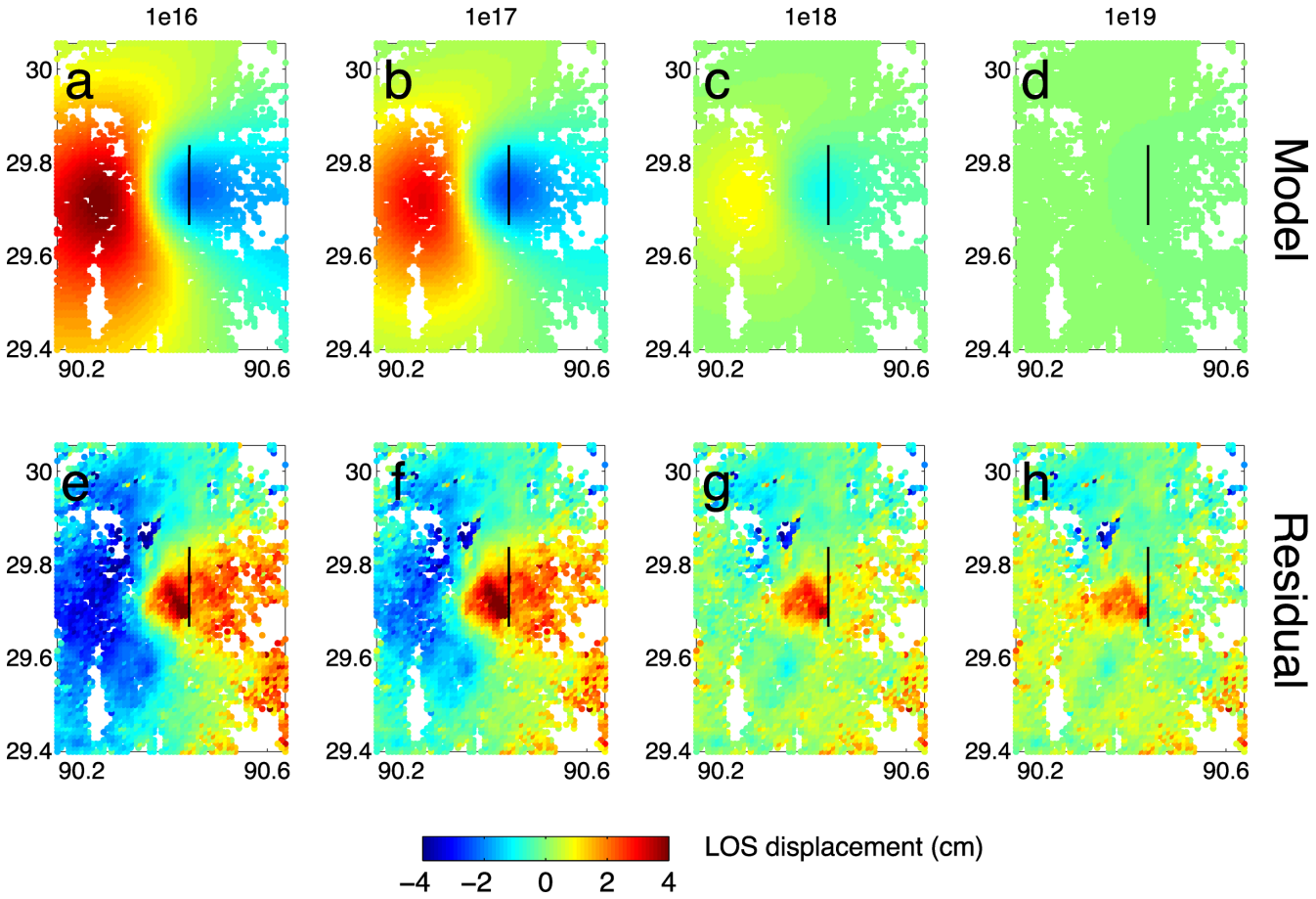

Figure 12. (a)–(d) Modelled post-seismic line-of-sight displacements due to viscoelastic relaxation at 615 d after the main shock, using variable viscosities (Pa s) marked as the title of each figure. (e)–(h) Residuals between the cumulative post-seismic deformation at 615 d after the main shock (subfigure titled 615 d in Fig. 5) and the modelled deformation due to viscoelastic relaxation in the mid/lower crust. Positive range change represents motion away from the satellite, while negative range change indicates motion towards the satellite.

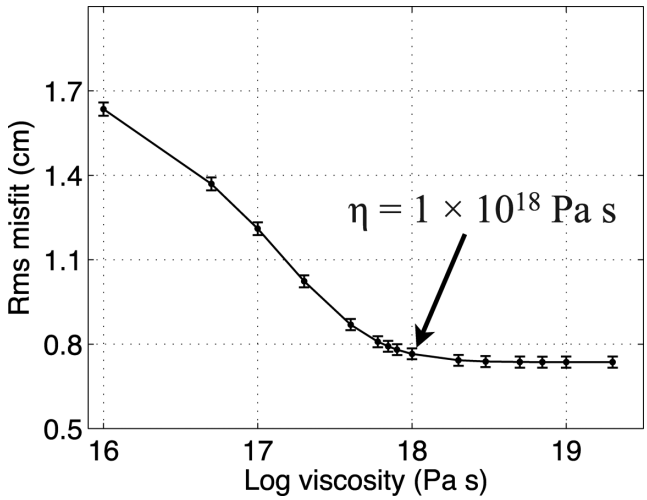

Figure 13. Plot of rms misfit versus log viscosity. Errors are the standard deviations of the rms misfit distributions derived by perturbing post-seismic deformation time-series with 100 sets of realistic noise, and rerunning 100 times the calculation of residual between modelled and observed displacements.

7 DISCUSSION

7.1 Layered crust versus homogeneous crust

The Damxung earthquake occurred in the north-central part of the Yadong-Gulu rift. The availability of seismic velocity estimates for the study area offers a chance to apply the layered crust model to derive earthquake source parameters. The INDEPTH II project carried out a thorough seismic survey along this part of the Tibetan Plateau, and there are many published results on the imaged crustal and/or mantle structure. These studies allow us to reasonably estimate the velocities. Lateral elasticity heterogeneity across the fault plane is left for further consideration.

Our uniform slip model assuming a homogeneous crust has similar source parameters as those obtained by other studies of this earthquake, as summarized by Liu *et al.* (2012) and shown in Table 1. When taking layering into consideration, the uniform slip model gives a different fault size (53.7 km^2 for layered crust versus 55.2 km^2 for homogeneous crust) and a slightly different slip direction (54.1° versus 54.8°). If we further derive distributed slip, both crustal models give spatially similar patterns of slip (Fig. 7). For the slip models with variable rake, the peak slip patch of the layered model locates at a depth of 7.7 km, and the maximum magnitude is 2.2 m, while for the homogeneous model, they are 6.9 and 2.4 m, respectively. This result is in accordance with the synthetic test by Hearn & Bürgmann (2005), highlighting the importance of

considering the layered characteristics of the crust. The seismic moment estimated for both crustal models are $\sim 3.60 \times 10^{18}$ N m, equivalent to a M_w 6.3 earthquake.

7.2 Coseismic slip, afterslip and aftershocks

It has been observed in previous studies of normal faulting events that afterslip tends to occur at the edges of the coseismic slip zone (Copley *et al.* 2012; D'Agostino *et al.* 2012). In this study, afterslip patch A (Fig. 9) appears in the upper layer of the layered elastic crust, which may represent the response of the shallow fault to stress change and/or redistribution of shallow material. Patches B and C sit near the upper and lower southern edges of the coseismic slip. We note that the afterslip under a downdip depth of 11 km is relatively poorly resolved, as revealed by the error analysis in Section 5.2. For this earthquake, none of the slip patches are much deeper than the coseismic slip, which is also the case for other normal faulting earthquakes studied geodetically, such as the 2009 M_w 6.3 L' Aquila earthquake (D' Agostino *et al.* 2012), the 2008 M_w 6.4 Nima-Gaize earthquake (Ryder *et al.* 2010), and the 1959 M_w 7.3 Hebgen Lake, Montana earthquake (Nishimura & Thatcher 2003). Together these might indicate that shallow afterslip is responsible for the near-field post-seismic displacement of normal faulting events. In general, the possibility of deep afterslip on the downdip extension of coseismic fault planes needs to be further investigated.

The three localized afterslip patches locate at different depths and are distributed along the fault, showing no obvious correlation with depth as suggested by the rate and state friction law (Tse & Rice 1986; Scholz 2002), according to which depth-dependent frictional properties should limit afterslip to above and below the main coseismic rupture. This inconsistency was also found in the study of the L'Aquila earthquake, and was interpreted as being caused by additional complexity of fault properties relative to a depth-dependent frictional model (D' Agostino *et al.* 2012). We infer that the frictional properties on the fault differ not only in the downdip direction, but also laterally along strike.

Given that we have no InSAR observations for the first 20 d of post-seismic deformation, we are not able to constrain the spatial pattern of afterslip in this very early phase, although we did a linear back projection of the post-seismic deformation. There are two possible scenarios for these first 20 d: (i) the afterslip is spatially stable, and similar to that for later epochs and (ii) the afterslip migrates following the main shock into surrounding regions. Studies on other earthquakes, such as the 2005 Nias-Simeulue earthquake (Hsu *et al*. 2006), the 2004 Parkfield earthquake (Johnson *et al*. 2006) and the 2011 Tohoku-Oki earthquake (Ozawa *et al.* 2012), show that afterslip inverted from very early post-seismic geodetic observation is generally spatially stable, and so we infer that the second scenario proposed above is less likely for the 2008 Damxung earthquake.

The temporal evolution of afterslip and aftershocks of the Damxung earthquake are different. Cumulative aftershock numbers decay faster than the cumulative line-of-sight deformation (Fig. 6). Similarly, Fig. 11 shows that the decaying rate of cumulative seismic moment calculated from the CEDC catalogue is faster than that of cumulative moment released by afterslip. The study of the 1999 Chi-Chi earthquake by Perfettini & Avouac (2004) suggests that afterslip governs the temporal evolution of aftershocks. This does not appear to hold for the Damxung earthquake, which may be a consequence of the different earthquake type (thrusting versus normal faulting), or the different fault zone environment.

7.3 Viscosity constraints for the deep crust of southern Tibet

InSAR measurements of post-seismic deformation provide a unique opportunity to study the mid/lower crustal rheology of Tibet. Post-seismic deformation for a number of earthquakes in Tibet has been effectively modelled to constrain the crustal and/or mantle strength of the plateau (Ryder *et al.* 2007, 2010, 2011; Wen *et al.* 2012). Ryder *et al.* (2007) modelled viscoelastic relaxation following the 1997 M_w 7.5 Manyi earthquake, and inferred an effective viscosity of $3–10 \times 10^{18}$ Pa s beneath a 15 km elastic layer. Studies by Ryder *et al.* (2011) and Wen *et al.* (2012) of the post-seismic transients following the 2001 M_w 7.9 Kokoxili earthquake found steady-state viscosities of about 10^{19} Pa s. A robust lower bound of 3×10^{17} Pa s was placed on the mid/lower crustal viscosity of central Tibet from modelling of viscoelastic relaxation in a Maxwell half-space following the 2008 Nima-Gaize earthquake (Ryder *et al.* 2010). The viscosities in the range of 3×10^{17}–2×10^{19} Pa s fall in the central part of the range of 10^{16}–10^{21} Pa s estimated for the plateau by modelling of present-day topography, margin relief of the Tibetan Plateau and GPS records of interseismic surface movement (Clark & Royden 2000; Shen *et al.* 2001; Clark *et al.* 2005; Copley & Mckenzie 2007; Bendick *et al.* 2008; Hilley *et al.* 2009; Zhang *et al.* 2009).

In this study, a lower bound of 1×10^{18} Pa s is inferred for the mid/lower crust viscosity of this part of the Yadong-Gulu rift, which is consistent with estimates for other parts of the plateau. We notice that several other moderate to large normal faulting earthquakes occurred along this rift since the last century, for example, the 1952 M 7.5 Gulu earthquake located at northern end of the rift and the 1992 M_w 6.2 Nyemu earthquake to the south of the 2008 Damxung earthquake. Modelling of InSAR-recorded late post-seismic deformation of these events would enable further probing of lithospheric rheology of different sections of this specific long-enduring seismic zone, and thus facilitate understanding of the earthquake cycle.

8 CONCLUSIONS

This study uses InSAR observations to investigate the coseismic and post-seismic surface deformation associated with the 2008 M_w 6.3 Damxung earthquake in Tibet. The coseismic deformation pattern revealed by InSAR confirms that a west-dipping normal fault on the eastern margin of the Yadong-Gulu rift is responsible for this event. Inversion of multiple Envisat data assuming both homogeneous and layered crustal models yields comparable coseismic slip distribution patterns, revealing a blind rupture below a downdip depth of $\sim$5 km. The maximum slip for the layered model is smaller and deeper, while the moment release values calculated from both models are similar ($\sim 3.60 \times 10^{18}$ N m). For the post-seismic period, localized line-of-sight increase in the hanging wall of the southern part of the rupture can be well reproduced by three afterslip patches located at different positions on the fault plane. Localized afterslip patches are located in the shallow upper crust and at the top and bottom edges of the coseismic slip, revealing frictional heterogeneities in both downdip and along-strike directions of the fault. Our afterslip model also excludes deep afterslip (>15 km) on the downdip extension of the fault. Afterslip moment within the first 615 d is at least $\sim$11 per cent of the moment released by coseismic slip. The temporal evolution of aftershocks and afterslip are not linearly correlated. By modelling viscoelastic relaxation in a Maxwell half-space, we place a lower bound of 1×10^{18} Pa s on the viscosity of the mid/lower crust of this part of the Yadong-Gulu rift. Continued post-seismic

deformation modelling of other normal faulting events that occurred along this rift system will allow for rheological strength mapping and earthquake risk assessment of this active seismic zone.

ACKNOWLEDGEMENTS

We thank the editor, Prof Duncan Agnew, and two anonymous reviewers for their constructive suggestions. Envisat SAR data are provided by the European Space Agency (ESA) through CAT–1 proposal (proposal ID C1P. 5119). Fig. 1 was generated using open-access software GeoMapApp. Lidong Bie acknowledges financial support from the University of Liverpool and the China Scholarship Council. We also thank Rongjiang Wang (GFZ Potsdam) for help with PSGRN/PSCMP installation, and the Seismology Group at the University of Liverpool for useful discussions.

REFERENCES

Amoruso, A., Crescentini, L. & Fidani, C., 2004. Effects of crustal layering on source parameter inversion from coseismic geodetic data, *Geophys. J. Int.,* **159**(1), 353–364.

Armijo, R., Tapponnier, P., Mercier, J.L. & Tong-Lin, H., 1986. Quaternary extension in southern Tibet: field observations and tectonic implications, *J. geophys. Res.,* **91**(B14), 13 803–13 872.

Barbot, S. & Fialko, Y., 2010. Fourier-domain Green's function for an elastic semi-infinite solid under gravity, with applications to earthquake and volcano deformation, *Geophys. J. Int.,* **182**(2), 568–582.

Barbot, S., Hamiel, Y. & Fialko, Y., 2008. Space geodetic investigation of the coseismic and postseismic deformation due to the 2003 M_w 7.2 Altai earthquake: implications for the local lithospheric rheology, *J. geophys. Res.,* **113**(B3), B03403, doi:10.1029/2007JB005063.

Barnhart, W.D. & Lohman, R.B., 2012. Regional trends in active diapirism revealed by mountain range-scale InSAR time series, *Geophys. Res. Lett.,* **39**(8), doi:10.1029/2012GL051255.

Barnhart, W.D. & Lohman, R.B., 2013. Phantom earthquakes and triggered aseismic creep: vertical portioning of strain during earthquake sequences in Iran, *Geophys. Res. Lett.,* **40,** 819–823.

Bendick, R., McKenzie, D. & Etienne, J., 2008. Topography associated with crustal flow in continental collisions, with application to Tibet, *Geophys. J. Int.,* **175**(1), 375–385.

Berardino, P., Fornaro, G., Lanari, R. & Sansosti, E., 2002. A new algorithm for surface deformation monitoring based on small baseline differential SAR interferograms, *IEEE Trans. Geosci. Remote Sens.,* **40**(11) 2375–2383.

Berteussen, K.A., 1977. Moho depth determinations based on spectral ratio analysis of NORSAR long period P waves, *Phys. Earth planet. Inter.,* **15,** 13–27.

Bürgmann, R., Ergintav, S., Segall, P., Hearn, E.H., McClusky, S., Reilinger, R.E., Woith, H. & Zschau, J., 2002. Time-dependent distributed afterslip on and deep below the Izmit earthquake rupture, *Bull. seism. Soc. Am.,* **92**(1), 126–137.

Cavalié, O., Doin, M.P., Lasserre, C. & Briole, P., 2007. Ground motion measurement in the Lake Mead area, Nevada, by differential synthetic aperture radar interferometry time series analysis: probing the lithosphere rheological structure, *J. geophys. Res.,* **112**(B3), B03403, doi:10.1029/2006JB004344.

Cavalié, O., Lasserre, C., Doin, M.P., Peltzer, G., Sun, J., Xu, X. & Shen, Z.K., 2008. Measurement of interseismic strain across the Haiyuan fault (Gansu, China), by InSAR, *Earth planet. Sci. Lett.,* **275**(3), 246–257.

Clark, M.K. & Royden, L.H., 2000. Topographic ooze: building the eastern margin of Tibet by lower crustal flow, *Geology,* **28**(8), 703–706.

Clark, M.K., House, M.A., Royden, L.H., Whipple, K.X., Burchfiel, B.C., Zhang, X. & Tang, W., 2005. Late Cenozoic uplift of southeastern Tibet, *Geology,* **33,** 525–528.

Copley, A. & McKenzie, D., 2007. Models of crustal flow in the India–Asia collision zone, *Geophys. J. Int.,* **169**(2), 683–698.

Copley, A., Hollingsworth, J. & Bergman, E., 2012. Constraints on fault and lithosphere rheology from the coseismic slip and postseismic afterslip of the 2006 M_w 7.0 Mozambique earthquake, *J. geophys. Res.,* **117**(B3), B03404, doi:10.1029/2011JB008580.

D'Agostino, N., Cheloni, D., Fornaro, G., Giuliani, R. & Reale, D., 2012. Space-time distribution of afterslip following the 2009 L'Aquila earthquake, *J. geophys. Res.,* **117**(B2), B02402, doi:10.1029/2011JB008523.

Devlin, S., Isacks, B.L., Pritchard, M.E., Barnhart, W.D. & Lohman, R.B., 2012. Depths and focal mechanisms of crustal earthquakes in the central Andes determined from teleseismic waveform analysis and InSAR, *Tectonics,* **31**(2), doi:10.1029/2011TC002914.

Deng, J., Gurnis, M., Kanamori, H. & Hauksson, E., 1998. Viscoelastic flow in the lower crust after the 1992 Landers, California, earthquake, *Science,* **282**(5394), 1689–1692.

Dieterich, J.H., 2007. Applications of rate- and state-dependent friction to models of fault slip and earthquake occurrence, *Treat. Geophys.,* **4,** 107–129.

Doin, M.P., Lasserre, C., Peltzer, G., Cavalié, O. & Doubre, C., 2009. Corrections of stratified tropospheric delays in SAR interferometry: validation with global atmospheric models, *J. appl. Geophys.,* **69**(1), 35–50.

Elliott, J.R., Walters, R.J., England, P.C., Jackson, J.A., Li, Z. & Parsons, B, 2010. Extension on the Tibetan plateau: recent normal faulting measured by InSAR and body wave seismology, *Geophys. J. Int.,* **183**(2), 503–535.

Farr, T.G. *et al.*, 2007. The Shuttle Radar Topography Mission, *Rev. Geophys.,* **45**(2), doi:10.1029/2005RG000183.

Fialko, Y., 2004. Probing the mechanical properties of seismically active crust with space geodesy: study of the coseismic deformation due to the 1992 Mw7. 3 Landers (southern California) earthquake, *J. geophys. Res.,* **109**(B3), doi:10.1029/2003JB002756.

Fialko, Y., Simons, M. & Agnew, D., 2001. The complete (3-D) surface displacement field in the epicentral area of the 1999 Mw7. 1 Hector Mine earthquake, California, from space geodetic observations, *Geophys. Res. Lett.,* **28**(16), 3063–3066.

Funning, G.J., Parsons, B., Wright, T.J., Jackson, J.A. & Fielding, E.J., 2005. Surface displacements and source parameters of the 2003 Bam (Iran) earthquake from Envisat advanced synthetic aperture radar imagery, *J. geophys. Res.,* **110**(B9), doi:10.1029/2004JB003338.

Goldstein, R.M., Zebker, H.A. & Werner, C.L., 1988. Satellite radar interferometry: Two-dimensional phase unwrapping, *Radio Sci.,* **23**(4), 713–720.

Gourmelen, N. & Amelung, F., 2005. Postseismic mantle relaxation in the central Nevada seismic belt, *Science,* **310**(5753), 1473–1476.

Gray, A.L., Mattar, K.E. & Sofko, G., 2000. Influence of ionospheric electron density fluctuations on satellite radar interferometry, *Geophys. Res. Lett.,* **27**(10), 1451–1454.

Hanssen, R.F., 2001. *Radar Interferometry: Data Interpretation and Error Analysis,* Kluwer.

Harris, R.A. & Segall, P., 1987. Detection of a locked zone at depth on the Parkfield, California, segment of the San Andreas fault, *J. geophys. Res.,* **92**(B8), 7945–7962.

Hearn, E.H. & Bürgmann, R., 2005. The effect of elastic layering on inversions of GPS data for coseismic slip and resulting stress changes: Strike-slip earthquakes, *Bull. seism. Soc. Am.,* **95**(5), 1637–1653.

Hilley, G.E., Johnson, K.M., Wang, M., Shen, Z.K. & Bürgmann, R., 2009. Earthquake–cycle deformation and fault slip rates in northern Tibet, *Geology,* **37**(1), 31–34.

Hoechner, A., Sobolev, S.V., Einarsson, I. & Wang, R., 2011. Investigation on afterslip and steady state and transient rheology based on postseismic deformation and geoid change caused by the Sumatra 2004 earthquake, *Geochem. Geophys. Geosyst.,* **12**(7), Q07010, doi:10.1029/2010GC003450.

Hsu, Y.J. *et al.*, 2006. Frictional afterslip following the 2005 Nias-Simeulue earthquake, Sumatra, *Science,* **312**(5782), 1921–1926.

Johanson, I.A., Fielding, E.J., Rolandone, F. & Bürgmann, R., 2006. Coseismic and postseismic slip of the 2004 Parkfield earthquake from space-geodetic data, *Bull. seism. Soc. Am.,* **96**(4B), S269–S282.

Johnson, K.M., Bürgmann, R. & Larson, K., 2006. Frictional properties on the San Andreas fault near Parkfield, California, inferred from models of

afterslip following the 2004 earthquake, *Bull. seism. Soc. Am.,* **96**(4B), S321–S338.

Jónsson, S., Zebker, H., Segall, P. & Amelung, F., 2002. Fault slip distribution of the 1999 M_w 7.1 Hector Mine, California, earthquake, estimated from satellite radar and GPS measurements, *Bull. seism. Soc. Am.,* **92**(4), 1377–1389.

Kind, R. *et al.*, 2002. Seismic images of crust and upper mantle beneath Tibet: Evidence for Eurasian plate subduction, *Science,* **298**(5596), 1219–1221.

Klemperer, S., 2006. Crustal flow in Tibet: Geophysical evidence for the physical state of Tibetan lithosphere, and inferred patterns of active flow, *Geol. Soc. Spec. Publ.,* **268,** 39–70.

Kola-Ojo, O. & Meissner, R., 2001. Southern Tibet: Its deep seismic structure and some tectonic implications, *J. Asian Earth Sci.,* **19**(1), 249–256.

Liu, Y., Xu, C., Wen, Y., He, P. & Jiang, G., 2012. Fault rupture model of the 2008 Dangxiong (Tibet, China) M_w 6.3 earthquake from Envisat and ALOS data, *Adv. Space Res.,* **50,** 952–956.

Lohman, R.B. & Simons, M., 2005. Some thoughts on the use of InSAR data to constrain models of surface deformation: Noise structure and data downsampling, *Geochem. Geophys. Geosyst.,* **6**(1), Q01007, doi:10.1029/2004GC000841.

Nelder, J.A. & Mead, R., 1965. A simplex method for function minimization, *Comput. J.,* **7**(4), 308–313.

Nelson, K.D. *et al.*, 1996. Partially molten middle crust beneath southern Tibet: synthesis of project INDEPTH results, *Science,* **274**(5293), 1684–1688.

Nishimura, T. & Thatcher, W., 2003. Rheology of the lithosphere inferred from postseismic uplift following the 1959 Hebgen Lake earthquake, *J. geophys. Res.,* **108**(B8), 2389, doi:10.1029/2002JB002191.

Okada, Y., 1985. Surface deformation due to shear and tensile faults in a half-space, *Bull. seism. Soc. Am.,* **75,** 1135–1154.

Owens, T.J. & Zandt, G., 1997. Implications of crustal property variations for models of Tibetan plateau evolution, *Nature,* **387**(6628), 37–43.

Ozawa, S., Nishimura, T., Munekane, H., Suito, H., Kobayashi, T., Tobita, M. & Imakiire, T., 2012. Preceding, coseismic, and postseismic slips of the 2011 Tohoku earthquake, Japan, *J. geophys. Res.,* **117**(B7), B07404, doi:10.1029/2011JB009120.

Peltzer, G., Rosen, P., Rogez, F. & Hudnut, K., 1996. Postseismic rebound in fault step-overs caused by pore fluid flow, *Science,* **273,** 1202–1204.

Perfettini, H. & Avouac, J.P., 2004. Postseismic relaxation driven by brittle creep: A possible mechanism to reconcile geodetic measurements and the decay rate of aftershocks, application to the Chi-Chi earthquake, Taiwan, *J. geophys. Res.,* **109**(B2), B02304, doi:10.129/2003JB002911.

Philibosian, B. & Simons, M., 2011. A survey of volcanic deformation on Java using ALOS PALSAR interferometric time series, *Geochem. Geophys. Geosyst.,* **12**(11), Q11004, doi:10.1029/2011GC003775.

Pollitz, F., 2005. Transient rheology of the upper mantle beneath central Alaska inferred from the crustal velocity field following the 2002 Denali earthquake, *J. geophys. Res.,* **110,** B08407, doi:10.1029/2005JB003672.

Rapine, R., Tilmann, F., West, M., Ni, J. & Rodgers, A., 2003. Crustal structure of northern and southern Tibet from surface wave dispersion analysis, *J. geophys. Res.,* **108**(B2), 2120, doi:10.1029/2001JB000445.

Rippe, D. & Unsworth, M., 2010. Quantifying crustal flow in Tibet with magnetotelluric data, *Phys. Earth planet. Inter.,* **179,** 107–121.

Riva, R.E.M., Borghi, A., Aoudia, A., Barzarghi, R., Sabadini, R. & Panza, G.F., 2007. Viscoelastic relaxation and long-lasting afterslip following the 1997 Umbria-Marche (central Italy) earthquakes, *Geophys. J. Int.,* **169,** 534–546.

Rosen, P.A., Hensley, S. & Peltzer, G., 2004. Updated repeat orbit interferometry package released, *EOS, Trans. Am. geophys. Un.,* **85**(5), 47.

Ryder, I., Parsons, B., Wright, T.J. & Funning, G.J., 2007. Post-seismic motion following the 1997 Manyi (Tibet) earthquake: InSAR observations and modelling, *Geophys. J. Int.,* **169**(3), 1009–1027.

Ryder, I., Bürgmann, R. & Sun, J., 2010. Tandem afterslip on connected fault planes following the 2008 Nima-Gaize (Tibet) earthquake, *J. geophys. Res.,* **115**(B3), B03404, doi:10.1029/2009JB006423.

Ryder, I., Bürgmann, R. & Pollitz, F., 2011. Lower crustal relaxation beneath the Tibetan Plateau and Qaidam Basin following the 2001 Kokoxili earthquake, *Geophys. J. Int.,* **187**(2), 613–630.

Sandwell, D.T., Sichoix, L. & Smith, B., 2002. The 1999 Hector Mine earthquake, southern California: Vector near-field displacements from ERS InSAR, *Bull. seism. Soc. Am.,* **92**(4), 1341–1354.

Savage, J.C., 1987. Effect of crustal layering upon dislocation modeling, *J. geophys. Res.,* **92**(B10), 10 595–10 600.

Schmidt, D.A. & Bürgmann, R., 2003. Time-dependent land uplift and subsidence in the Santa Clara valley, California, from a large interferometric synthetic aperture radar data set, *J. geophys. Res.,* **108**(B9), 2416, doi:10.1029/2002JB002267.

Scholz, C.H., 2002. *The Mechanics of Earthquakes and Faulting,* Cambridge Univ. Press.

Shen, Z.K., Wang, M., Li, Y., Jackson, D.B., Yin, A., Dong, D. & Fang, P., 2001. Crustal deformation along the Altyn Tagh fault system, western China, from GPS, *J. geophys. Res.,* **106**(B12), 30 607–30 621.

Simons, M., Fialko, Y. & Rivera, L., 2002. Coseismic deformation from the 1999 M_w 7.1 Hector Mine, California, earthquake as inferred from InSAR and GPS observations, *Bull. seism. Soc. Am.,* **92**(4), 1390–1402.

Styron, R., Taylor, M. & Okoronkwo, K., 2010. Database of active structures from the Indo-Asian collision, *EOS, Trans. Am. Geophys. Un.,* **91**(20), 181–182.

Sun, J., Johnson, K.M., Cao, Z., Shen, Z., Bürgmann, R. & Xu, X, 2011. Mechanical constraints on inversion of coseismic geodetic data for fault slip and geometry: Example from InSAR observation of the 6 October 2008 M_w 6.3 Dangxiong-Yangyi (Tibet) earthquake, *J. geophys. Res.,* **116**(B1), B01406, doi:10.1029/2010JB007849.

Tse, S.T. & Rice, J.R., 1986. Crustal earthquake instability in relation to the depth variation of frictional slip properties, *J. geophys. Res,* **91**(B9), 9452–9472.

Wald, D.J., Heaton, T.H. & Hudnut, K.W., 1996. The slip history of the 1994 Northridge, California, earthquake determined from strong-motion, teleseismic, GPS, and leveling data, *Bull. seism. Soc. Am.,* **86**(1B), S49–S70.

Wang, R., Martín, F.L. & Roth, F., 2003. Computation of deformation induced by earthquakes in a multi-layered elastic crust-FORTRAN programs EDGRN/EDCMP, *Comput. Geosci.,* **29**(2), 195–207.

Wang, R., Martín, F.L. & Roth, F., 2006. PSGRN/PSCMP–a new code for calculating co-and post-seismic deformation, geoid and gravity changes based on the viscoelastic-gravitational dislocation theory, *Comput. Geosci.,* **32**(4), 527–541.

Wen, Y., Li, Z., Xu, C., Ryder, I. & Bürgmann, R., 2012. Postseismic motion after the 2001 M_w 7.8 Kokoxili earthquake in Tibet observed by InSAR time series, *J. geophys. Res.,* **117**(B8), B08405, doi:10.1029/2011JB009043.

Wright, T.J., Parsons, B., Jackson, J., Haynes, M., Fielding, E., England, P. & Clarke, P., 1999. Source parameters of the 1 October 1995 Dinar (Turkey) earthquake from SAR interferometry and seismic body wave modelling, *Earth planet. Sci. Lett.,* **172,** 23–37.

Wright, T.J., Lu, Z. & Wicks, C., 2003. Source model for the M_w 6.7, 23 October 2002, Nenana Mountain earthquake (Alaska) from InSAR, *Geophys. Res. Lett.,* **30**(18), 1974, doi:10.1029/2003GL018014.

Wu, Z.H., Ye, P.S., Barosh, P.J. & Wu, Z.H., 2011. The October 6, 2008 M_w 6.3 magnitude Damxung earthquake, Yadong-Gulu rift, Tibet, and implications for present-day crustal deformation within Tibet, *J. Asian Earth Sci.,* **40**(4), 943–957.

Xiong, X., Shan, B., Zheng, Y. & Wang, R., 2010. Stress transfer and its implication for earthquake hazard on the Kunlun Fault, Tibet, *Tectonophysics,* **482**(1), 216–225.

Yamasaki, T. & Houseman, G.A., 2012. The crustal viscosity gradient measured from post-seismic deformation: a case study of the 1997 Manyi (Tibet) earthquake, *Earth planet. Sci. Lett.,* **351,** 105–114.

Yuan, X., Ni, J., Kind, R., Mechie, J. & Sandvol, E., 1997. Lithospheric and upper mantle structure of southern Tibet from a seismological passive source experiment, *J. geophys. Res.,* **102,** 27 491–27 500.

Zebker, H.A., Rosen, P.A. & Hensley, S., 1997. Atmospheric effects in interferometric synthetic aperture radar surface deformation and topographic maps, *J. geophys. Res.,* **102**(B10), 7547–7563.

Zhang, C., Cao, J. & Shi, Y., 2009. Studying the viscosity of lower crust of Qinghai-Tibet Plateau according to post-seismic deformation, *Sci. China, Ser. D,* **52**(3), 411–419.

Zhao, S., Müller, R.D., Takahashi, Y. & Kaneda, Y., 2004. 3-D finite-element modelling of deformation and stress associated with faulting: effect of inhomogeneous crustal structures, *Geophys. J. Int.,* **157**(2), 629–644.

SUPPORTING INFORMATION

Additional Supporting Information may be found in the online version of this article:

Figure S1. Ascending interferogram track 26. Positive range change represents motion away from the satellite, while negative range change indicates motion towards the satellite.

Figure S2. Tradeoffs and uncertainties of source parameters for the uniform slip model assuming a homogeneous crust. Red curves in the last row are the Gaussian fit to the distribution of source parameters. Unit of each parameter is the same as that in Table 1.

Figure S3. Resolution test employing a checkerboard pattern. Left-hand side is the input slip distribution and right side is the recovered slip distribution.

Figure S4. Tradeoffs and uncertainties of synthetic source parameters (Table S2) for the uniform slip model assuming a layered crust. 100 synthetic noise perturbed datasets are inverted for source parameters distribution. Red curves in the last row are the Gaussian fit to the distribution of source parameters. Unit of each parameter is the same as that in Table 1.

Figure S5. Tradeoffs and uncertainties of source parameters for the uniform slip model assuming a layered crust. Red curves in the last row are the Gaussian fit to the distribution of source parameters. Unit of each parameter is the same as that in Table 1.

Figure S6. Modelled post-seismic deformation time-series from afterslip distribution shown in Fig. 9. Black line represents the fault trace inferred in this study. Title of each subfigure refers to number of days after earthquake on 6 October 2008.

Figure S7. Residual between the original post-seismic deformation time-series (Fig. 5) and the forward-modelled post-seismic deformation time-series (Fig. S6). Title of each subfigure refers to number of days after earthquake on 6 October 2008.

Figure S8. Afterslip errors at each SAR acquisition. Error here is the standard deviation of the afterslip distributions derived by inverting 100 sets of realistic noise perturbed post-seismic deformation time-series.

Table S1. Envisat aquisitions (a) and interferograms (b) used in this study for the 2008 Damxung earthquake.

Table S2. Synthetic input source parameters and inversion results for the test of simulated annealing and downhill simplex algorithm considering the effects of crustal layering. A rectangular normal fault buried beneath 4 km with uniform slip of 5 m is used to forward model surface displacements. Displacements are perturbed with synthetic noise and inverted for source parameters using the improved algorithm. Location and fault geometry parameters are well retrieved.

Table S3. Coseismic variable-slip model in a layered crust in Finite Source Parameter (FSP) format.

Table S4a–k. Post-seismic fixed-rake slip models in a layered crust in FSP format (attached as separate text files, the number at the end of each title denotes the days since the main shock).
(http://gji.oxfordjournals.org/lookup/suppl/doi:10.1093/gji/ggt444/-/DC1)

Please note: Oxford University Press is not responsible for the content or functionality of any supporting materials supplied by the authors. Any queries (other than missing material) should be directed to the corresponding author for the article.